



## LASER ALLOYING OF ZINC WITH ALUMINUM: SOLIDIFICATION BEHAVIOR

P. A. CARVALHO, A. M. DEUS, R. COLAÇO and R. VILAR

Departamento de Engenharia de Materiais, Instituto Superior Técnico, Av. Rovisco Pais, 1096 Lisboa,  
Portugal

(Received 22 April 1996; accepted 18 July 1997)

**Abstract**—Laser alloyed tracks were produced by blowing aluminum powder into melt pools generated in zinc substrates. Analysis of the microstructures revealed a structural and compositional stratification related with a deficient aluminum redistribution in the liquid. The effect of chemical heterogeneity on solidification mechanisms was modeled. The composition gradients and the solidification undercooling were shown to strongly influence the geometry of the solidification front. A reasonable agreement was obtained between experimental and predicted characteristic dimensions of the microstructures, in particular, the radii of the dendrite tips observed experimentally were comparable to the calculated ones. © 1997 Acta Metallurgica Inc.

### 1. INTRODUCTION

In laser surface alloying the high energy of a laser beam is used to alloy the surface of a material with another material. Usually, the alloying elements are injected in the form of a powder into the melt pool created in the substrate by the laser beam [1]. If variable powder feed rates are used, the chemical composition along the tracks can be changed and this enables a rapid and exhaustive preparation of a whole range of alloys. Some work has been reported on rapid alloy prototyping using laser processing with variable powder feed rates: Monson *et al.* [2] studied the microstructure and hardness evolution vs composition variation for two alloy systems (Ni–Cr–Si–C–B and Mo–Ni–Cr–Si–C–B–Fe); Abbas *et al.* [3] investigated the wear behavior of variable composition stellite–SiC laser clad deposits and Carvalho *et al.* [4] systematically evaluated the corrosion behavior of Co–Ni–Al alloy grades. In the present work, laser alloying of zinc with aluminum was performed by injecting aluminum powder, at variable and constant feed rates, into melt pools generated in zinc substrates. The aim was to prepare a large number of Zn–Al homogeneous alloys, so that the potential of these alloys as sacrificial coating materials for the protection of steel against corrosion could be systematically investigated. However, in all the tracks produced a structural and compositional stratification was observed, which was related to a deficient aluminum redistribution in the liquid.

In recent years, several studies have been published on the distribution of alloying elements in laser surface alloying [5–12], and in some of them significant depthwise chemical heterogeneities were reported [8–10]. In these cases, the variety of solidi-

fication structures found in the treated layers is explained in terms of a deficient distribution of the alloying elements. However, the effect of composition gradients on the solidification mechanisms is analyzed only in a qualitative manner. Furthermore, although concentration fields based on flow patterns have been thoroughly modeled [5, 10, 11], the effect of chemical heterogeneity on the geometry of the solidification front (and consequently on the solidification rate [13]) seems to have never been investigated. In this study, the influence of composition gradients on solidification mechanisms was modeled and some computations were carried out in order to evaluate the influence of chemical heterogeneity on the geometry of the solidification front.

### 2. EXPERIMENTAL PROCEDURE

The experiments were performed with a 3 KW continuous wave CO<sub>2</sub> laser. The mode of the laser beam was a mixture of TEM<sub>00</sub> with higher order modes (specially TEM<sub>01</sub><sup>\*</sup>). An argon jet, coaxial with the beam, was used to shield the melt pool from oxygen and to protect the optics from fumes and spattered metal. The substrates were moved under the stationary laser beam by a numerically controlled X–Y table. A computer controlled powder feeder (described elsewhere [4]) supplied the aluminum powder to the melt pools. The alloyed tracks were made with a laser beam power of 1500 W, a 3.8 mm beam diameter and a traverse speed of 5 mm/s, which resulted in an energy density of 100 MJ/m<sup>2</sup>. The powder was delivered to the melt pool by an argon jet with a 25 cm<sup>3</sup>/s flow rate. The injection nozzle, whose internal diameter was 1.5 mm,

made an angle of  $45^\circ$  to the substrate surface, and had its extremity at a distance of 18 mm from the center of the irradiated region. The aluminum powder had 99.5 wt% purity and a particle size below  $250\ \mu\text{m}$ . The substrates were 99.99 wt% zinc. Due to the substantial increase in zinc vapor pressure on heating, the shielding and injection gas was also used to remove from the laser beam path some of the vapors formed. Some tracks were made with the aluminum powder feed rate varying from 0 to 0.06 g/s, while others were made with the following constant feed rates: 0.01, 0.03, 0.045 and 0.06 g/s. The length of the tracks with a variable composition was 10 cm.

Detailed microstructural analyses were performed using standard metallographic methods. The specimens were etched in an aqueous solution of chromic acid and sodium sulfate. An optimal contrast in optical microscopy was obtained with polarized light. The chemical analyses were performed with a microprobe in representative regions of  $10^4\ \mu\text{m}^2$ . Dendritic and lamellar spacings were measured on enlarged SEM prints of tracks produced with a constant powder feed rate of 0.06 g/s. The measurement of the lamellar spacing was performed in transverse cross-sections. The experimental value was obtained from the number of intersections with 25 lines of  $2\ \mu\text{m}$  in length, which were drawn perpendicular to the orientation of the lamellas. The dendritic spacings were measured in transverse and longitudinal cross-sections of the tracks, the experimental values obtained are the average of 30 measurements.

### 3. EXPERIMENTAL RESULTS

Figure 1 shows a typical example of the microstructures found in transverse cross-sections of the alloyed tracks. Solidification structures presenting three well defined layers were always observed. Examination at higher magnifications enabled to resolve a dendritic zone at the top [Fig. 2(a) and (b)], another dendritic zone at the bottom [Fig. 2(d)] and eutectic lamellas grouped in cells at the intermediate region [Fig. 2(c) and (d)]. The results obtained with variable powder feed rates were similar to those achieved with constant powder feed rates; however, the thickness of the intermediate and top layers tended to increase with increasing powder feed rate, whereas the inverse happened to the thickness of the bottom layer.

Figure 3 shows a longitudinal cross-section of a track produced with a constant powder feed rate of 0.06 g/s. The cellular nature of the intermediate layer eutectic can clearly be seen in Fig. 3(b); the angle between the growth direction of the eutectic cells and the beam scanning direction ( $\theta_{\text{eu}}$ ) was found to be  $21 \pm 3^\circ$  (average of 30 measurements). As can be observed in Fig. 3(b) and (c), growth was quite unconstrained at the top dendritic layer.

Longitudinal bands parallel to the solidification front were observed at the bottom dendritic layer [Fig. 3(a)]. Chemical composition profiles obtained in representative regions of this cross-section are presented in Fig. 4. Some tips of bottom layer dendrites, which were situated close to the intermediate layer, can be seen in Fig. 5.

Table 1 contains experimental primary and secondary arm spacings of the  $\alpha_{\text{Zn}}$  and  $\beta_{\text{Al}}$  dendrites as well as the lamellar spacing of the intermediate layer eutectic. The measurement of the lamellar spacing was performed all over the eutectic layer. The dendritic spacings were measured in regions near the eutectic layer.

### 4. MICROSTRUCTURE ANALYSIS

To understand the microstructures obtained it was necessary to know what phases could appear during the solidification of Zn–Al alloys and the modifications induced on the solidification structures by possible solid-state transformations. The Zn–Al equilibrium phase diagram presents a simple eutectic configuration [14] and according to several previous studies [15–19] the solidification of Zn–Al alloys does not involve the formation of non-equilibrium phases, even for growth rates as high as 160 mm/s [15]. Furthermore, the solid-state transformations which occur in this system do not significantly modify the solidification structures [16–19]. This information enables us to discuss the solidification process from the observed microstructures.

At the bottom of the trace, solidification started by epitaxial growth from the partially molten zinc grains (detail in Fig. 1). A constitutional undercooling was soon generated and, in consequence, the planar solid/liquid interface became unstable. This led to the onset of a dendritic structure of the zinc rich phase (primary  $\alpha_{\text{Zn}}$ ) with aluminum being rejected to the interdendritic zones, where a lamellar eutectic ( $\alpha_{\text{Zn}} + \beta_{\text{Al}}$ ) was finally formed [Fig. 2(d)].

Banded configurations similar to the one observed at the bottom dendritic layer [Fig. 3(a)] are common at scanning rates below 10 mm/s [20–22]. According to Gremaud [21], the banding behavior at low scanning rates is related to growth instabilities induced by convection. The observed bands, although irregular, define successive positions of the solidification front at the zinc rich layer.

The microstructures indicate that in the top layer solidification began either by heterogeneous nucleation on the surface oxides or by epitaxial growth from small aluminum particles, which were not completely dissolved and floated at the top of the pool. It can be seen in Fig. 3(a) that some of these nuclei grew in all directions and sometimes even developed in the direction opposite to the laser scanning direction [Fig. 3(b) and (c)]. Therefore,

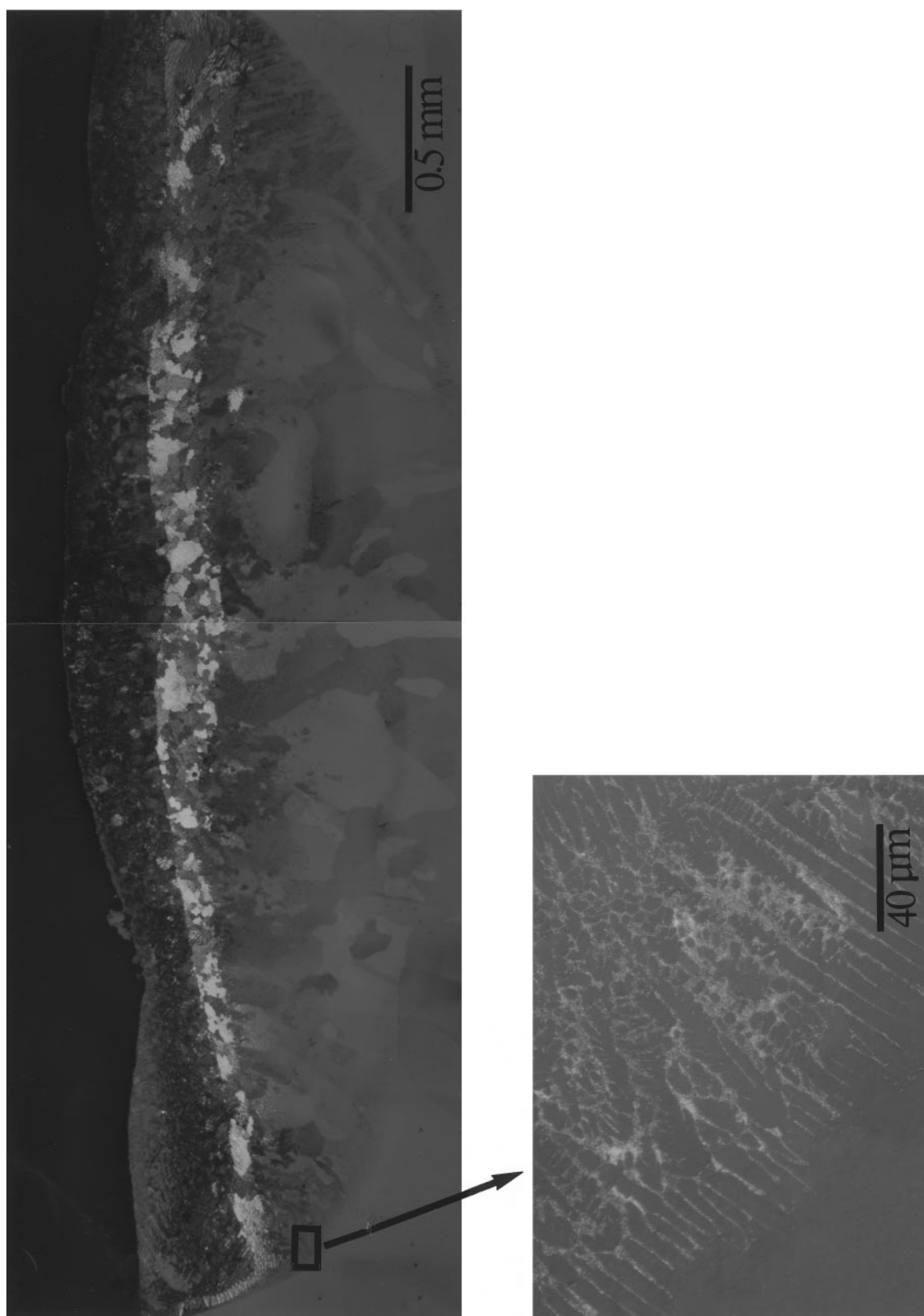


Fig. 1. Transverse cross-section of a track obtained with the aluminum powder feed rate varying continuously from 0 to 0.06 g/s. Since sectioning was performed at 8.9 cm from the beginning of the track, the nominal powder feed rate was 0.05 g/s. The treated region presents a well defined three-layer structure. Evidence of epitaxial growth can be seen in the detail of the bottom layer. The photomicrographs were obtained with polarized light in optical microscopy.

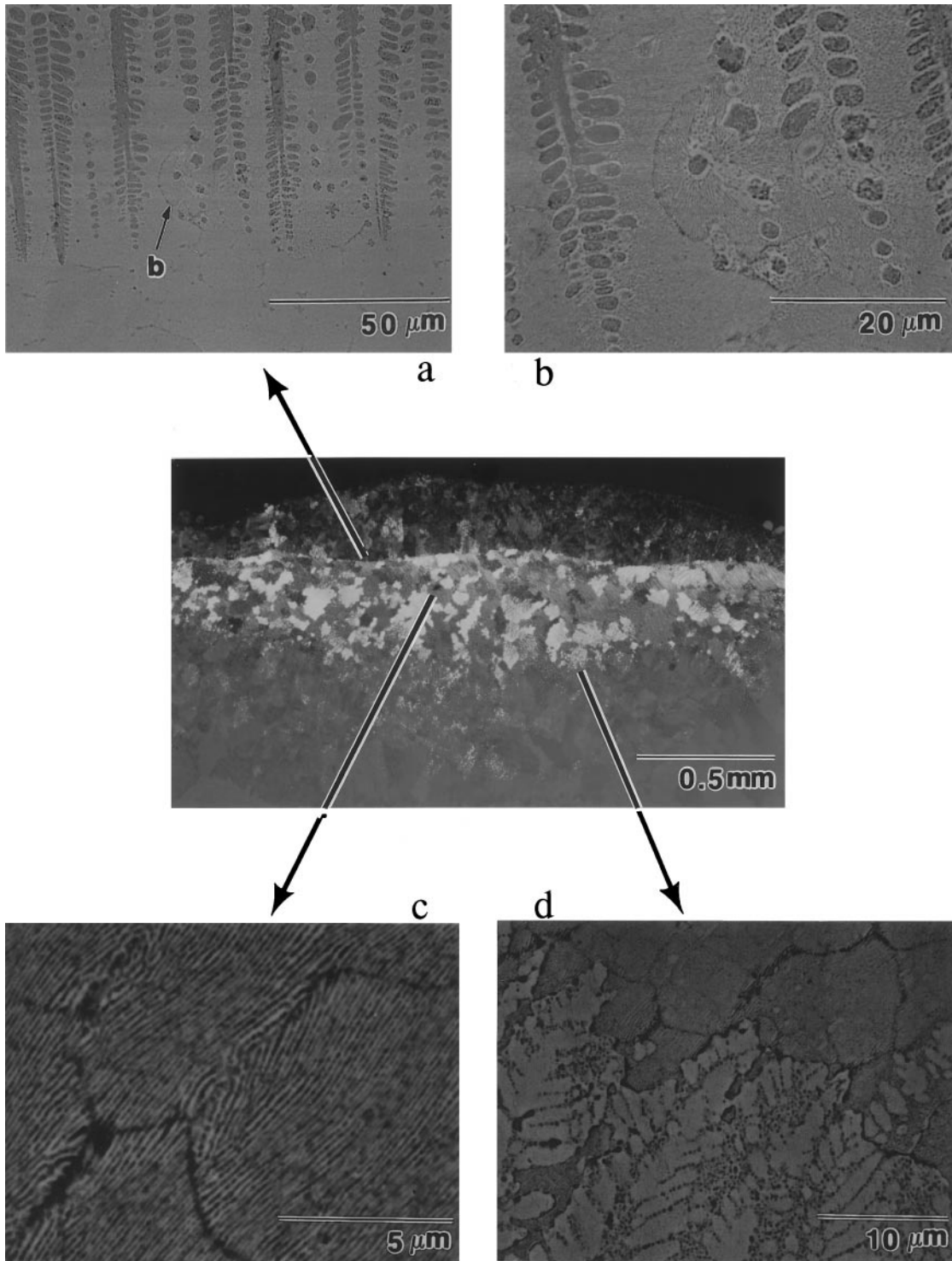


Fig. 2. Transverse cross-section of a track obtained with the aluminum powder feed rate varying continuously from 0 to 0.06 g/s. Since sectioning was performed at the end of the track, the nominal powder feed rate was 0.06 g/s: (a) top dendritic layer near the cellular region; (b) detail of (a); (c) cellular intermediate layer; (d) bottom dendritic layer near the cellular region.

growth was not strongly conditioned by the advancement of the isotherms and could occur in an almost unconstrained way in the melt. The latent heat of solidification seems to have been mainly dis-

sipated through the liquid, implying a thermally undercooled melt. This solidification behavior led to the formation of a dendritic structure of primary  $\beta_{Al}$ , with zinc being rejected to the interdendritic

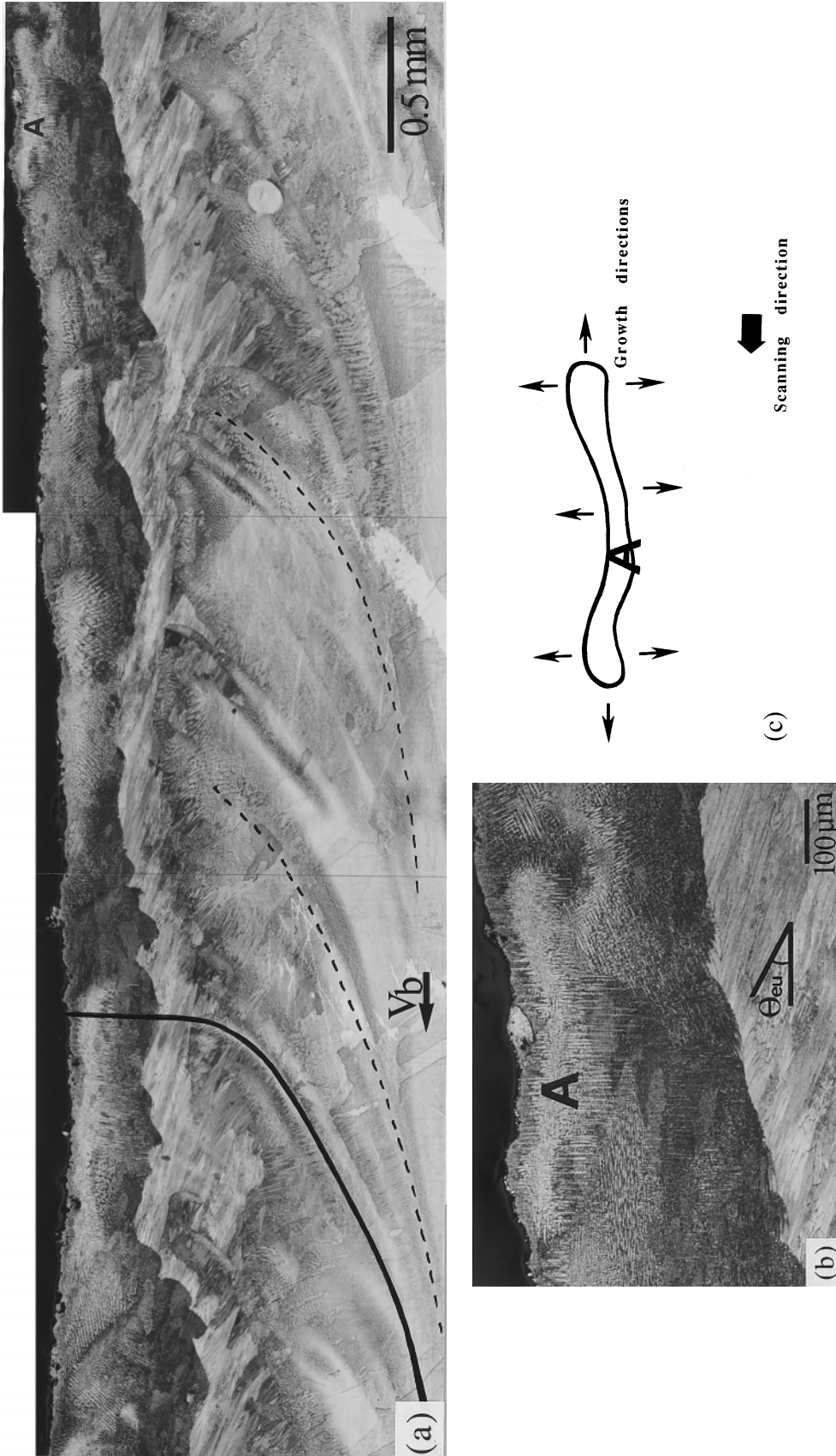


Fig. 3. (a) Longitudinal cross-section of a track obtained with a constant powder feed rate of 0.06 g/s. The beam scanned the specimen at a rate ( $V_b$ ) of 5 mm/s in the direction indicated by the arrow. Chemical analyses were performed along the path defined by the thick line; the composition profiles obtained are presented in Fig. 4. Some of the bands observed at the bottom dendritic layer are marked with dashed lines. To avoid vertical fluctuations of composition, the chemical analyses at the bottom layer were obtained along one of the observed bands; (b) detail of the top dendritic layer showing a nucleus of Al rich dendrites growing in all directions. The angle between the growth

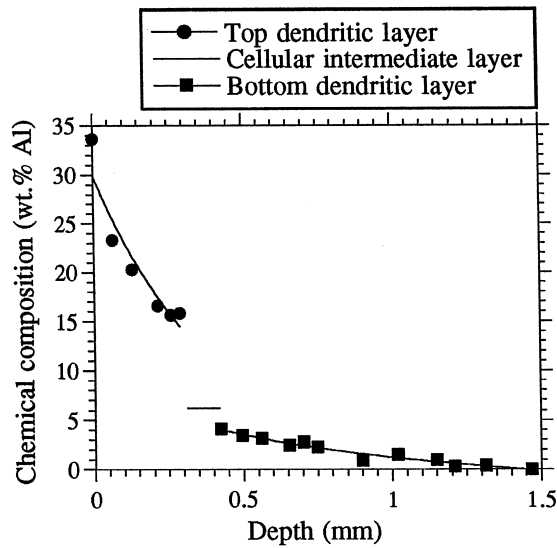


Fig. 4. Aluminum concentration profiles obtained in a longitudinal cross-section ( $y = 0$ ) of a track produced with a constant aluminum powder feed rate of 0.06 g/s [see Fig. 3(a)]. All values were determined from areas of  $10^4 \mu\text{m}^2$ . The Al content in the intermediate layer was fairly constant and an average value ( $6.2 \pm 0.8$  wt% Al for 11 measurements) is represented.

zones, where a lamellar/rod eutectic ( $\alpha_{\text{Zn}} + \beta_{\text{Al}}$ ) appeared at the end of solidification [Fig. 2(b)]. Since growth could occur in all directions, it can be inferred that solidification of  $\beta_{\text{Al}}$  started in regions not very far from the center of the irradiated area. Heterogeneous nucleation (or epitaxial growth) at the surface of the melt is not common in laser materials processing, but it has been observed in some cases [23, 24].

A cellular eutectic structure was observed at the intermediate layer [Fig. 2(c) and (d) and 3(a)], suggesting a prior cellular eutectic/liquid interface. Hence, segregation of impurities by both eutectic phases ( $\alpha_{\text{Zn}}$  and  $\beta_{\text{Al}}$ ) produced a diffusion boundary layer ahead of the eutectic/liquid interface, which induced a constitutional undercooling and promoted cellular type instabilities. In contrast to the other two layers, the composition in the intermedi-

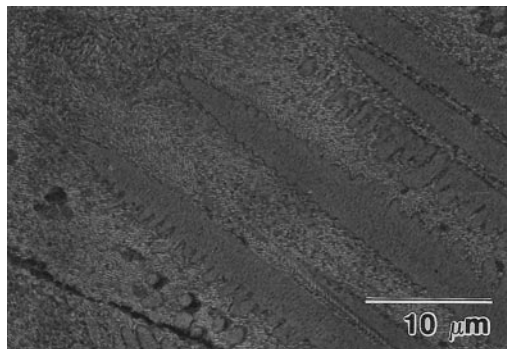


Fig. 5. Longitudinal cross-section showing  $\alpha_{\text{Zn}}$  dendrites parallel to the section plane.

ate region was fairly constant ( $6.2 \pm 0.8$  wt% Al) and no particular variation along the depth was observed (Fig. 4). The growth direction of the eutectic cells was also very uniform ( $\theta_{\text{eu}} = 21 \pm 3^\circ$ ).

The observed structures attest to an independent solidification behavior for each layer. Furthermore, the orientation of the dendrites (Fig. 3) indicates that solidification involved opposite moving fronts, i.e. while an  $\alpha_{\text{Zn}}$  dendritic front was advancing from the bottom, another phase ( $\beta_{\text{Al}}$ ) was growing at the melt top (a more comprehensive discussion on this type of solidification behavior can be found in [12]). A melt pool shape compatible with the microstructure orientation is presented diagrammatically in Fig. 6. The lines defining the solidification front represent the position of the dendrites and the cells' tips; fluctuations in composition and speed may have produced local irregularities.

Surface tension gradients, arising from temperature and composition gradients, are the main driving force for convective flow in laser materials processing [25], and this thermocapillarity induced convection is usually sufficiently intense to cause efficient solute redistributions in laser alloying [5, 13, 26]. However, the marked compositional stratification (Fig. 4) indicates that the existing fluid flow was unable to completely blend the Al rich liquid situated on top with the Zn rich liquid which was underneath. It should be noted that in dendritic growth segregation is essentially lateral, therefore the chemical heterogeneity observed could not have been caused by segregation occurring during solidification of the bottom and top dendritic layers. The difference in density between the injected material and the substrate strongly contributed to the lack of chemical homogeneity; simple calculations show that the upward acceleration of an aluminum particle in a zinc bath, resultant from buoyancy vs gravity effects, can be as high as  $16 \text{ m/s}^2$  ( $\Delta\rho/\rho_{\text{Al}} \cdot g$ , the density values used were obtained from [27]). Moreover, the encumbering presence of  $\beta_{\text{Al}}$  nuclei at the melt top tended to reduce the intensity of the thermocapillarity convection in the back part of the melt pool, affecting its stirring efficiency. Hence, the higher melting temperature of aluminum, as compared to the zinc melting point, also contributed to hinder homogenization by promoting a premature solidification at the surface. On the other hand, for the melt times involved in the process (of the order of 1 s) the diffusion distances in the melt pool were a few tens of microns; therefore, diffusion was responsible in a rather limited way for Al redistribution.

In principle, the use of higher energy densities would have increased the temperature gradients, intensifying surface tension disparities. As a result, in regions of the melt pool not covered by the  $\beta_{\text{Al}}$  solid cap, a stronger thermocapillarity induced convection would have been generated, promoting a better distribution of aluminum. However, in prac-

Table 1. Primary and secondary dendrite arm spacings (respectively  $\lambda_1$  and  $\lambda_2$ ) and lamellar eutectic spacing ( $\lambda$ ). All the experimental values were measured on tracks obtained with constant 0.06 g/s powder feed rates

	$\beta_{Al}$ dendrites		$\alpha_{Zn}$ dendrites		Lamellar eutectic
	$\lambda_1$ ( $\mu\text{m}$ )	$\lambda_2$ ( $\mu\text{m}$ )	$\lambda_1$ ( $\mu\text{m}$ )	$\lambda_2$ ( $\mu\text{m}$ )	$\lambda$ ( $\mu\text{m}$ )
Experimental	$14.4 \pm 3.4$	$2.0 \pm 0.4$	$10.3 \pm 2.2$	$1.7 \pm 0.3$	$0.154 \pm 0.03$
Calculated	—	—	12.0	2.9	0.12–0.17

tice, it was impossible to deliver more energy to the bath because of the low boiling temperature of zinc. Extremely violent vaporizations were found to occur for energy densities higher than  $100 \text{ MJ/m}^2$ . The addition of small quantities of surface active elements is known to substantially increase surface tension gradients [13, 26]. Hence, if surfactants had been used, chemical stratification might have been attenuated.

The experimental results obtained indicate that unsatisfactory homogenizations may be expected in laser surface alloying, when the injected element has a significantly higher melting point and a lower density than the substrate. In such cases, the buoyancy forces resulting from the difference in density between the injected material and the substrate contribute to a deficient distribution of the alloying elements, and the premature solidification, which can occur at the top of the bath, tends to reduce the stirring efficiency of thermocapillarity induced convection.

##### 5. INFLUENCE OF COMPOSITION HETEROGENEITY ON THE SOLIDIFICATION FRONT GEOMETRY

In order to describe the influence of chemical heterogeneity on the solidification mechanisms, each

point of the laser treated region was regarded as an individual alloy with a specific chemical composition. The temperature field was established using Ashby and Easterling's model [28] and the position of the liquidus temperatures in the melt pool was determined with basis on the experimental composition distribution. Subsequently, the solidification undercoolings at the  $\alpha_{Zn}$  dendritic layer were calculated using Kurz, Giovanola and Trivedi's model [29] and this enabled to determine the position of the solidification front at the bottom dendritic layer. Details on the calculations are given in the Appendix. Since the  $\beta_{Al}$  dendrites grew unconstrained at the melt top, it was impossible in practice to determine their growth rates. Consequently, the corresponding growth undercoolings were not calculated and the geometry of the solidification front at the top dendritic layer was not determined.

“Effective thermal conductivities“ have been used to account for the real shape of the melt pool, when heat conduction models are employed to define the temperature field [30, 31]. In this work, the geometry of the solidification front, calculated for the bottom dendritic layer, was made to coincide with the range of experimental shapes [Fig. 3(a)] by iteratively modifying the temperature field using thermal conductivity as adjusting parameter. The scheme in Fig. 7 represents the iterative compu-

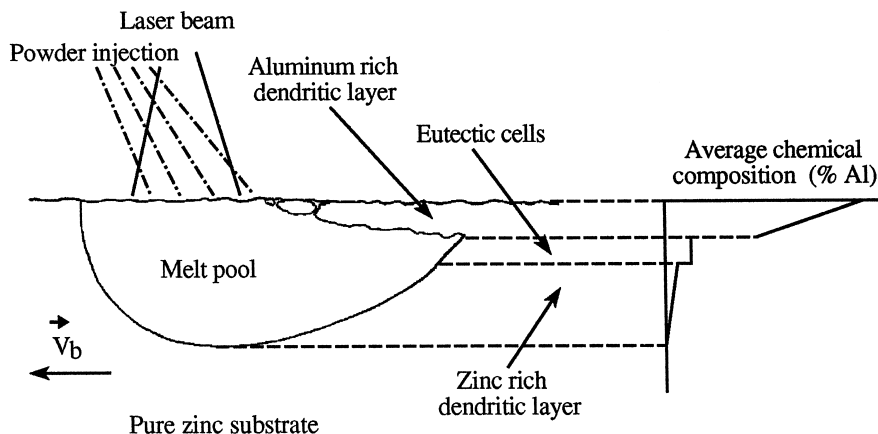


Fig. 6. Diagram representing a longitudinal cross-section of the melt pool, in which opposite moving solidification fronts can be seen. The direction of the beam scanning velocity ( $\bar{V}_b$ ) is indicated. At the bottom of the trace solidification started by epitaxial growth of the partially molten zinc grains. In the top layer solidification began either by heterogeneous nucleation on the surface oxides or by epitaxial growth from small undissolved aluminum particles. The essentially random orientation of the top layer dendrites attests to the unconstrained growth of each nucleus. The intermediate layer solidified with a cellular eutectic structure and the growth direction of the eutectic cells was quite uniform.

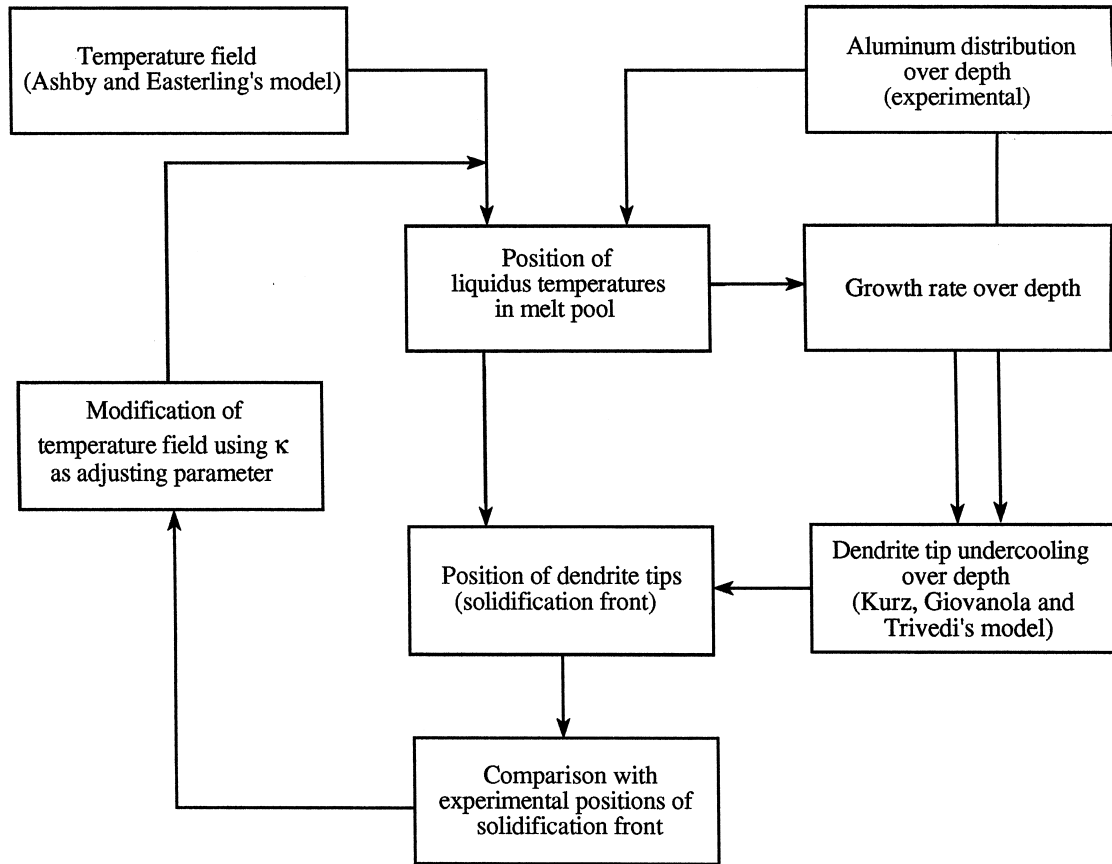


Fig. 7. Scheme of the iterative calculations performed to calibrate the temperature field.

tations which were performed to make the theoretical position of the  $\alpha_{Zn}$  dendritic front lie within the experimental range. This procedure aimed a satisfactory calibration of the temperature distribution using the experimental geometry of the solidification front as reference.

### 5.1. Results of the computations

Figure 8 shows the calculated position of the  $\alpha_{Zn}$  dendrite tips at the  $y = 0$  plane, as well as the range of experimental positions of the  $\alpha_{Zn}$  solidification front. Figure 9 presents the position of the liquidus temperature front. The isotherms corresponding to the Zn melting temperature, to the

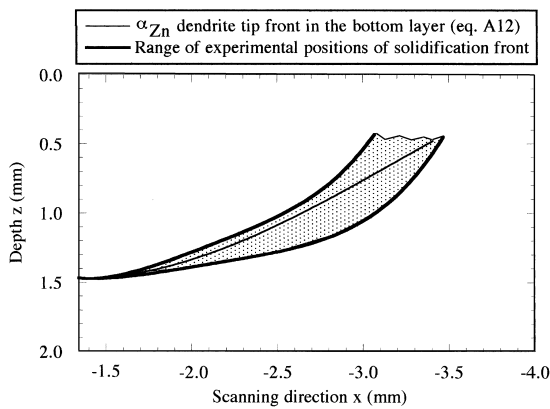


Fig. 8. Calculated position of the  $\alpha_{Zn}$  dendrite tips at the bottom layer. A range of experimental positions is also presented. The experimental curves were all made to coincide at the average measured depth of the 0.06 g/s tracks ( $1.47 \pm 0.22$  mm).

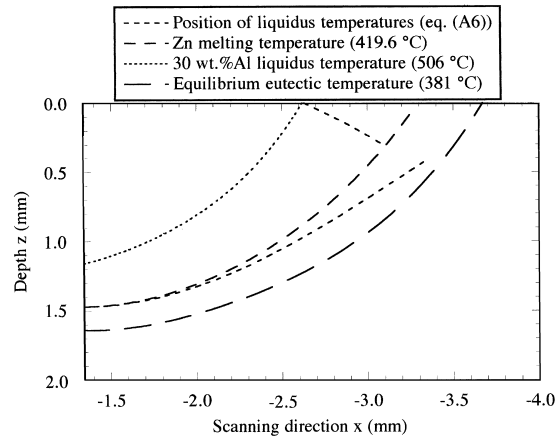


Fig. 9. Calculated positions of the liquidus temperatures in the melt pool. Three isotherms are shown as reference.

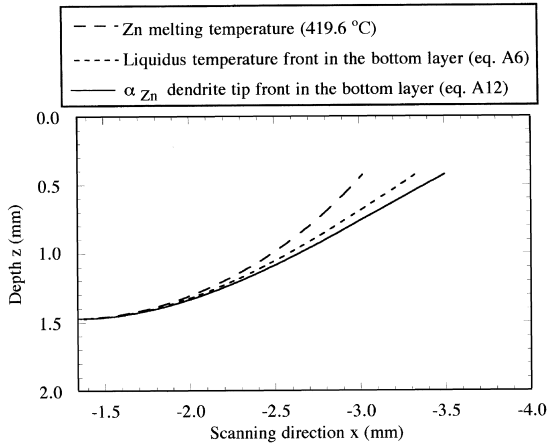


Fig. 10. Relative positions of the zinc melting temperature, liquidus temperature front, and  $\alpha_{Zn}$  solidification front.

equilibrium eutectic temperature and to the equilibrium liquidus temperature of the alloy with 33 wt% Al (composition measured at the surface) are also represented in Fig. 9. The effect of liquidus temperature variation and undercooling variation on the position of the  $\alpha_{Zn}$  dendritic front can be evaluated in Fig. 10. The calculated values of dendrite tip radius and undercooling, which were used to determine the position of the  $\alpha_{Zn}$  dendrite tips, reflected the influence of composition and growth rate variation over the depth [equation (A7)]. The undercooling determined for the top of the  $\alpha_{Zn}$  den-

dritic layer was 15°C and corresponded to a calculated tip radius of 0.3 mm.

The chemical composition profiles presented in Fig. 4 indicate that at the melt top the position of the liquidus temperature tended towards the isotherm corresponding to the equilibrium eutectic temperature as  $z$  increased and, conversely, at the bottom of the pool the position of the liquidus temperature approached the eutectic isotherm as  $z$  decreased (as can be seen in Fig. 9). Thus, assuming an aluminum distribution in the liquid similar to one found in the treated layer, the heterogeneous aluminum distribution led to a contraction of the melt pool at the top layer and to a lengthening at the bottom layer (as depicted in Fig. 6). By comparing the position of the liquidus temperatures with the position of the zinc melting isotherm (Fig. 9), it can be inferred that the variation of liquidus temperature across the depth had a large influence on the geometry of the solidification front. The relative positions of the liquidus temperature front and of the  $\alpha_{Zn}$  dendritic front (Fig. 10) reveal that solidification undercooling had also a significant effect on the geometry of the solidification front. The liquidus temperature variation and the solidification undercooling accounted for 23% of the total length of the solidification front at the zinc rich layer. These results show that chemical heterogeneity and solidification undercooling can strongly influence

Table A1. Physical properties and parameters used in the calculations

Symbol	Definition	Value	Units	Source
$r_0$	Beam radius at $z = 0$	$1.9 \times 10^{-3}$	m	Experimental
$P$	Laser beam power	1500	W	Experimental
$V_b$	Beam scanning rate	$5 \times 10^{-3}$	m/s	Experimental
$T_0$	Substrate initial temperature	20	°C	Experimental
$\rho$	Density	$6.62 \times 10^3$	kg/m <sup>3</sup>	[27]
$c_p$	Specific heat	$0.52 \times 10^3$	J/kg/K	[27]
$a_z$	Constant	-3.3	wt% Al	equation (A4)
$b_z$	Constant	$3.6 \times 10^{-5}$	m <sup>2</sup> (wt% Al)	equation (A4)
$a_\beta$	Constant	-34.0	wt% Al	equation (A4)
$b_\beta$	Constant	$2.1 \times 10^{-4}$	m <sup>2</sup> (wt% Al)	equation (A4)
$m_z^\alpha$	Liquidus slope for the $\alpha_{Zn}$ phase	-7.7	K/(wt% Al)	[14]
$T_z^\alpha$	Intercept for the $\alpha_{Zn}$ phase ( $T_{Zn}$ )	419.6	°C	[14]
$m_\beta^\beta$	Liquidus slope for the $\beta_{Al}$ phase	4.85	K/(wt% Al)	[14]
$T_\beta^\beta$	Intercept for the $\beta_{Al}$ phase	357	°C	[14]
$D$	Diffusion coefficient in the liquid	$2.04 \times 10^{-9}$	m <sup>2</sup> /s	[37]
$k$	$\alpha_{Zn}$ equilibrium partition coefficient	0.24	—	[14]
$m_z^\beta$	Solidus slope for the $\alpha_{Zn}$ phase	-32.2	K/(wt% Al)	[14]
$T$	Cooling rate (at $z = 0.425$ mm)	-461	K/s	equation (A1)
$G$	Temperature gradient (at $z = 0.425$ mm)	$1.48 \times 10^5$	K/m	equation (A1)
$\Delta T$	Tip-root temperature difference	7.7	K	[14]
$C$	Composition of the last liquid to solidify	5	wt% Al	[14]
$C_0$	Concentration at the top of bottom layer	$4.0 \pm 0.6$	wt% Al	Experimental
$\theta_z$	Growth angle of $\alpha_{Zn}$ (at $z = 0.425$ mm)	$28 \pm 5$	degree	Experimental
$V\alpha$	$\alpha_{Zn}$ dendrites growth rate (at $z = 0.425$ mm)	$4.4 \times 10^{-3}$	m/s	equation (A10)
$\Gamma_z^\alpha$	$\alpha_{Zn}$ phase Gibbs-Thompson coefficient	$1.1 \times 10^{-7}$	Km	[38]
$\Gamma^\beta$	$\beta_{Al}$ phase Gibbs-Thompson coefficient	$0.9 \times 10^{-7}$	Km	[38]
$m_{eu}^\alpha$	Liquidus slope for $\alpha_{Zn}$ at eutectic point	-7.7	K/(wt% Al)	[14]
$m_{eu}^\beta$	Liquidus slope for $\beta_{Al}$ at eutectic point	10.1	K/(wt% Al)	[14]
$\Delta C$	Length of eutectic equilibrium tie line	15.7	wt% Al	[14]
$f$	Eutectic volume fraction of $\alpha_{Zn}$ at $T_{eu}$	0.68	—	Estimated
$\Phi_z$	$\alpha$ eutectic cusp angle	30–80	degree	Estimated
$\Phi_\beta$	$\beta$ eutectic cusp angle	30–80	degree	Estimated
$\theta_{eu}$	Growth angle (Fig. 3(b))	$21 \pm 3$	degree	Experimental
$V_{eu}$	Eutectic cells growth rate	$4.7 \times 10^{-3}$	m/s	equation (A10)

the geometry of the solidification front, changing the local growth rate.

### 5.2. Experimental confirmation

The arm spacings of the  $\alpha_{Zn}$  dendrites were calculated for regions adjacent to the intermediate layer. The primary and secondary dendrite arm spacings ( $\lambda_1$  and  $\lambda_2$ ) were calculated, respectively with Kurz and Fisher's [32] and Feurer and Wunderlin's [33] models. The eutectic spacing at the intermediate layer was determined using Jackson and Hunt's model [34]. Since the growth rate of the  $\beta_{Al}$  dendrites could not be determined, the corresponding interdendritic spacings were not calculated. All parameters and properties used to calculate the theoretical spacings are listed in Table A1 (Appendix). The calculated primary and secondary arm spacings of the  $\alpha_{Zn}$  dendrites as well as the lamellar spacing of the intermediate layer eutectic are presented in Table 1. Jackson and Hunt's model also enabled to obtain the following results:  $4^\circ\text{C} < \Delta T_{eu} < 6^\circ\text{C}$  and  $7 \mu\text{m}^{3/2} \text{s}^{-1/2} < \lambda V_{eu}^{1/2} < 10 \mu\text{m}^{3/2} \text{s}^{-1/2}$ . The temperature at the eutectic front was found to lie between  $375$  and  $377^\circ\text{C}$  ( $T_{eu} - \Delta T_{eu}$ ), which is in agreement with the temperature determined for the  $\alpha_{Zn}$  dendrite tips situated nearby ( $T_{m_{zn}} + C_0 m_x^1 - \Delta T_t = 374^\circ\text{C}$ ).

A reasonable agreement was obtained between the experimental spacings and the theoretical predictions (Table 1). In the case of  $\lambda_1$  and  $\lambda_2$  this agreement attests to the acceptable simulation of the temperature field, from which some of the parameters used in the calculations ( $G$  and  $T$ ) were derived. As for  $\lambda$ , the experimental confirmation of the theoretical value corroborates the mean undercooling determined for the eutectic layer ( $\Delta T_{eu}$ ). Liu and Jones presented in [17] the eutectic coupled zone for the Zn–Al system and, according to these authors, a 6.2 wt% Al alloy should solidify with a lamellar structure for a 4.7 mm/s growth rate (see Table A1). The calculated values for  $\lambda V_{eu}^{1/2}$  are similar to the value presented by Liu and Jones in [17] for the 5 wt% Al alloy ( $7.1 \mu\text{m}^{3/2} \text{s}^{-1/2}$ ). The undercooling at the  $\alpha_{Zn}$  dendrite tips was determined as a function of the theoretical tip radius [equation (A7)]. Therefore, since in regions adjacent to the intermediate layer the  $\alpha_{Zn}$  dendrite tips were visible (Fig. 5), by comparing the tip radius calculated for that region,  $0.3 \mu\text{m}$ , with the dimensions of the observed tips, it was possible to indirectly assess the propriety of the undercooling established for that depth,  $15^\circ\text{C}$ .

As the temperature field was calculated with a simple heat conduction model, some important physical processes were not taken into consideration. In fact, Ashby and Easterling's model does not incorporate the effect of phase changes, therefore the discontinuity of heat flux across the moving interface, owing to phase transitions, was ignored. Furthermore, the effect of thermal conductivity

variation due to chemical and temperature heterogeneity was not evaluated and the existing fluid flow was neglected. Several numerical models have been developed to take proper account of some of these physical processes. However, the influence of the composition variation and the influence of the  $\beta_{Al}$  solid cap on heat conduction and on fluid dynamics cannot be easily treated. On the other hand, the use of a simple heat conduction model and its subsequent calibration (Fig. 7) seem to have resulted in an acceptable simulation of the temperature distribution, since the predicted values of  $\lambda_1$  and  $\lambda_2$  are in reasonable agreement with the ones obtained experimentally.

In the calculation of  $\Delta T_t(z)$ , in spite of the composition and growth rate variations over the depth, each point of the solidification front was treated as an individual alloy, which was not affected by the behavior of its neighborhood. Steady-state conditions were assumed, ignoring the fluctuations in solidification speed which caused the banded structure [Fig. 3(a)]. Moreover, the average growth direction of the dendrites was assumed to be perpendicular to the liquidus temperature front, consequently, no crystallographic considerations were taken into account in the determination of the dendritic growth rates. However, in spite of these assumptions and simplifications, the solidification behavior of the  $\alpha_{Zn}$  dendrites seems to have been reasonably described since the radii of the tips observed experimentally were comparable to the calculated ones.

## 6. CONCLUDING REMARKS

The structural and compositional stratification observed was a consequence of the deficient Al redistribution in the melt. The experimental results indicate that homogenization may be difficult in systems where the injected element has a higher melting point and a lower density than the substrate. In such cases, thermocapillarity induced convection can be impeded if the top of the bath starts to solidify (due to its higher melting point) and the buoyancy forces, resulting from the difference in density between the injected material and the substrate, contribute to stratification. Chemical heterogeneity and the dendritic undercooling were found to have a strong influence on the shape and position of the solidification front. A reasonable agreement was obtained between the experimental and predicted characteristic dimensions of the microstructure. The undercooling determined for the  $\alpha_{Zn}$  dendrite tips (near the intermediate region) corresponded to calculated tip radii comparable to the dimensions of the tips observed experimentally. In the case of  $\lambda_1$  and  $\lambda_2$ , the agreement between the theoretical and the experimental values attested to the *acceptable* simulation of the temperature distribution.

## REFERENCES

1. Draper, C. W. and Poate, J. M., *Int. Mater. Rev.*, 1985, **30**, 85.
2. Monson, P. J. E., Steen, W. M. and West, D. R. F., in *Proc. Inter. Conf. on Lasers Advanced Materials Processing* ed. Y. Arata. High Temperature Society of Japan, Osaka 1987, p. 377.
3. Abbas, G., West, D. R. F. and Steen, W. M., in *Surface Engineering with High Energy Beams* ed. A. P. Loureiro, O. Conde, L. Guerra-Rosa and R. Vilar. Trans Tech Publications, Aedermannsdorf 1990, p. 447.
4. Carvalho, P. A., Braz, N., Pontinha, M. M., Ferreira, M. G. S., Steen, W. M., Vilar, R. and Watkins, K. G., *Surf. Coat. Tech.*, 1995, **72**, 62.
5. Chande, T. and Mazumder, J., *J. Appl. Phys.*, 1985, **57**, 2226.
6. Gaffet, E., Pelletier, J. M. and Bonnet-Jobez, S., *Acta metall.*, 1989, **37**, 3205.
7. Kostrubiec, K., *J. Mater. Sci.*, 1991, **26**, 6044.
8. Dey, G. K., Kulkarni, U. D., Batra, I. and Banerjee, S., *Acta metall. mater.*, 1994, **42**, 2973.
9. Das, D. K., Prasad, K. S. and Paradkar, A. G., *Mater. Sci. Eng. A*, 1994, **174**, 75.
10. Smurov, I. and Ignatiev, M., in *NATO ASI Serie E-307* ed. J. Mazumder, O. Conde, R. Vilar and W. Steen. Kluwer Academic Publishers, Dordrecht, The Netherlands 1996, p. 267.
11. Pirch, N., Kreutz, E. W., Ollier, B. and He, X., in *NATO ASI Serie E-307* ed. J. Mazumder, O. Conde, R. Vilar and W. Steen. Kluwer Academic Publishers, Dordrecht, The Netherlands 1996, p. 177.
12. Carvalho, P. A. and Vilar, R., *Surf. Coat. Tech.* 1997, **91**, 158.
13. David, S. A. and Vitek, J. M., *Int. Mat. Rev.*, 1989, **34**, 213.
14. Mey, S., *Z. Metallkd.*, 1993, **84**, 451.
15. Livingstone, J. D., Cline, H. E., Koch, E. F. and Russell, R. R., *Acta metall.*, 1970, **18**, 399.
16. Lasek, J., Bartuska, P., Synecek, V. and Simerska, M., *Lasers in Engineering*, 1991, **1**, 111.
17. Liu, H. L. and Jones, H., *Acta metall. mater.*, 1992, **40**, 2003.
18. Synecek, V., Bartuska, P., Lasek, J. and Simerska, M., *Z. Metallkd.*, 1992, **83**, 245.
19. Zhu, Y. H., *J. Mater. Res.*, 1996, **11**, 593.
20. Munitz, A., *Metall. Trans. B*, 1985, **16**, 149.
21. Gremaud, M., *Ph.D. thesis 885.*, Swiss Federal Institut of Technology-Lausanne, 1990.
22. Gremaud, M., Carrard, M. and Kurz, W., *Acta metall. mater.*, 1990, **38**, 2587.
23. Bergmann, H. M., Barton, G., Mordike, B. L. and Fritsch, H. V., in *Proc. of Rapidly Solidified Metastable Materials* ed. B. H. Kear and B. C. Giessen. Materials Research Society Symposia Proceedings, Elsevier, New York 1984, p. 29.
24. Almeida, A., Que, Y. Y. and Vilar, R., *Scripta metall. mater.*, 1995, **33**, 863.
25. Chan, C., Mazumder, J. and Chen, M. M., *Metall. Trans. A*, 1984, **15**, 2175.
26. Mundra, K., Debroy, T., Zacharia, T. and David, S., *Weld. Res. Suppl.*, 1992, **9**, 313–s.
27. *Metals Handbook*, Vol. 2, 10th Ed. ASM, Metals Park, OH, 1992.
28. Ashby, M. F. and Easterling, K. E., *Acta metall.*, 1984, **32**, 195.
29. Kurz, W., Giovanola, B. and Trivedi, R., *Acta metall.*, 1986, **34**, 823.
30. Apps, R. L. and Milner, D. R., *Brit. Weld. J.*, 1963, **10**, 348.
31. Chande, T. and Mazumder, J., *J. Appl. Phys. Letters*, 1982, **41**, 42.
32. Kurz, W. and Fisher, D. J., *Acta metall.*, 1981, **29**, 11.
33. Feurer, U. and Wunderlin, K., *Einfluss der Zusammensetzung und der Erstarrungsbedingungen auf Die Dendritenmorphologie Binarer Al-Legierungen*. Fachbericht der Deutschen Gesellschaft für Metallkunde, Oberursel, Germany, 1977.
34. Jackson, K. A. and Hunt, J. D., *Trans. Metall. Soc. AIME*, 1966, **236**, 1129.
35. Bradley, J. R., *J. Phys. D: Appl. Phys.*, 1988, **21**, 834.
36. Ivantsov, G. P., *Dokl. Akad. Nauk. SSSR.*, 1947, **58**, 567.
37. Trivedi, R. and Kurz, W., *Int. Mater. Rev.*, 1994, **39**, 49.
38. Liu, H. Y. and Jones, H., *Acta metall. mater.*, 1992, **40**, 229.

## APPENDIX

*Modeling the influence of composition heterogeneity on solidification mechanisms*

*Establishing the temperature field*

Ashby and Easterling [28] showed that the solution to the heat conduction equation, for the case of a laser beam tracking the surface of a solid, can be well approximated by a simple analytical equation. According to these authors, in steady state and for  $x \gg r_0^2 V_b / 4\alpha$ , the equation for a  $T_1$  isotherm in the medial plane of the track ( $y = 0$ ) plane is given by:

$$T(z, x) = T_0 + \left(\frac{AP}{2\pi\kappa}\right) \frac{1}{x} \exp\left(-\frac{V_b(z+z_0)^2}{4\alpha x}\right) \quad (\text{A1})$$

with

$$z_0 = \sqrt{\frac{r_0}{e} \sqrt{\frac{\pi\alpha r_0}{V_b}}} \quad (\text{A2})$$

where  $t$  is the time,  $r_0$  is the beam half-width,  $\alpha$  is the thermal diffusivity,  $T$  is the temperature,  $z$  is the depth below surface,  $V_b$  is the laser beam scanning velocity,  $x$  is the scanning direction ( $x = V_b t$ ),  $T_0$  is the initial temperature of the substrate,  $A$  is the absorptivity,  $P$  is the beam power and  $\kappa$  is the thermal conductivity.

The values of the parameters and properties used in the calculation of the temperature field are listed in Table A1. Owing to the lack of suitable data for Zn–Al alloys, the values of the physical properties used, except thermal conductivity and the absorption coefficient, were those for liquid zinc at melting temperature. Absorptivity was established by making the maximum depth of the calculated zinc melting isotherm (419.6°C [14]) match the depth of the traces. The depth of the traces produced with a constant powder feed rate of 0.06 g/s was  $1.47 \pm 0.22$  mm (30 measurements) and the maximum value of the 419.6°C isotherm corresponded to this experimental molten depth for an absorptivity value of 0.17. This type of procedure has been used to establish the “absorption coefficient” when the fraction of absorbed energy cannot be reasonably determined [21, 35].

The geometry of the solidification front, calculated for the bottom layer, was made to coincide with the range of experimental shapes defined by the banded structure [Fig. 3(a)]. This was done by iteratively modifying the calculated temperature field, using thermal conductivity as adjusting parameter. A good agreement was obtained with  $\kappa = 28$  W/m/K; the process was initialized with  $\kappa = 60$  W/m/K, which is the thermal conductivity for pure zinc [27]. The condition  $x \gg r_0^2 V_b / 4\alpha$  was valid for the region studied.

*Determining the position of the liquidus temperature front*

Since the chemical composition variation over the depth  $C_0(z)$  was known (Fig. 4), the position of the equilibrium liquidus temperatures ( $T_i$ ) in the  $y = 0$  plane could be established from the Zn–Al equilibrium phase diagram and the temperature field:

$$T_1^i[C_0^i(z)] = T(z, x) \quad (\text{A3})$$

with  $T(z, x)$  being given by equation (A1) and  $i$  corresponding to each dendritic layer; being  $\alpha$  for the bottom layer and  $\beta$  for the top layer. The following equation was fitted to the experimental composition profiles obtained at the dendritic layers:

$$C_0^i(z) = a_i + \frac{b_i}{(z + z_0)^2} \quad (\text{A4})$$

where  $a_i$  and  $b_i$  are constants and  $i$  corresponds to the top or the bottom layer. The curves are presented in Fig. 4 together with the experimental data. In the case of linear liquidus lines:

$$T_1^i[C_0^i(z)] = T_*^i + m_1^i C_0^i(z) \quad (\text{A5})$$

where  $m_1^i$  are the liquidus slopes and  $T_*^i$  are the intercepts for 0 wt% Al. Since equation (A5) is not in a tractable form, it was modified to the following equivalent system:

$$(z + z_0)^2 = \frac{\frac{AP}{2\pi\kappa} \varphi \exp\left(-\frac{V_b}{4z}\right) - m_1^i b_i}{T_*^i + m_1^i a_i - T_0} \quad (\text{A6})$$

$$x = \frac{(z + z_0)^2}{\varphi}$$

which was solved using  $\varphi$  as a free parameter. The position of the liquidus temperatures in the melt pool was then given by equation (A6) (Fig. 9). The use of equation (A4) as the composition fitting curve enabled to solve equation (A5); good correlation was obtained ( $r_\alpha = 0.978$  and  $r_\beta = 0.947$ ) showing that this approach was plausible. All the values of parameters and physical properties used in the calculations can be found in Table A1.

*Determining the position of the  $\alpha_{Zn}$  solidification front*

In directional or constrained growth, if the local equilibrium condition is satisfied, the dendrite tip undercooling  $\Delta T_i$  can be given by [36, 37]:

$$\Delta T_i = \Delta T_s + \Delta T_R = \frac{k\Delta T_0 \text{Iv}(\text{Pe})}{1 - (1 - k)\text{Iv}(\text{Pe})} + \frac{2\Gamma}{R} \quad (\text{A7})$$

with

$$\text{Pe} = \frac{RV}{2D} \quad \text{and} \quad \text{Iv}(\text{Pe}) = \text{Pe} \cdot \exp(\text{Pe}) E(\text{Pe}) \quad (\text{A8})$$

where  $\Delta T_s$  is the undercooling required for solute diffu-

sion,  $\Delta T_R$  is the undercooling due to capillarity effects,  $\Gamma$  is the Gibbs–Thompson coefficient,  $R$  is the dendrite tip radius,  $k$  is the equilibrium partition coefficient,  $\Delta T_0$  is the liquidus–solidus range,  $\text{Pe}$  is the Péclet number for solute diffusion,  $V$  is the dendrite tip velocity,  $D$  is the solute diffusion coefficient in the liquid and  $E(\text{Pe})$  is the exponential integral function.

Kurz, Giovanola and Trivedi [29] proposed the following relationship for constrained dendritic growth with well defined secondary arms at moderate growth rates:

$$R = \sqrt{\frac{4\pi^2 \Gamma D [1 - (1 - k)\text{Iv}(\text{Pe})]}{\Delta T_0 V k}} \quad (\text{A9})$$

The undercooling at the  $\alpha_{Zn}$  dendrite tips was calculated using equation (A7). Since equations (A8) and (A9) are strongly interrelated, an iterative method was used to find the values of  $R$  and  $\text{Pe}$  at each depth. The calculations were initialized with  $R = 10^{-7} \mu\text{m}$ . All physical properties and parameters were considered to be constant (Table A1), except  $\Delta T_0$  and  $V$ , which varied continuously with the depth. The  $\Delta T_0$  values were determined from linearization of the  $\alpha_{Zn}$  liquidus and solidus lines; the correspondence with  $z$  was made through the chemical composition  $C_0^i(z)$ , given by equation (A4). It was assumed that on average the growth direction of the  $\alpha_{Zn}$  dendrites was perpendicular to the liquidus temperature front and the values of  $V(z)$  were calculated from:

$$V = V_b \cos \theta \quad (\text{A10})$$

where  $\theta$  is the angle between the scanning direction and the normal to the liquidus temperature front. The values taken by  $\theta$  at each depth were determined from the local slope of the curve defined by equation (A6). The values of  $\text{Iv}(\text{Pe})$  were obtained numerically.

The position of the  $\alpha_{Zn}$  dendrite tips in the  $y = 0$  plane is then given by the following equation:

$$T_1^z[C_0^z(z)] - \Delta T_i(z) = T(z, x) \quad (\text{A11})$$

which is equivalent to:

$$(z + z_0)^2 = \frac{\frac{AP}{2\pi\kappa} \varphi \exp\left(-\frac{V_b}{4z} \varphi\right) - m_1^z b_z}{T_*^z + m_1^z a_z - T_0 - \Delta T_i(z)} \quad (\text{A12})$$

$$x = \frac{(z + z_0)^2}{\varphi}$$

Twenty-five experimental curves, which defined successive longitudinal positions of the solidification front at the  $\alpha_{Zn}$  dendritic layer, were digitalized from photomicrographs of tracks produced with constant 0.06 g/s powder feed rates. The position of the  $\alpha_{Zn}$  dendrite tips, given by equation (A12), was made to lie within the range of experimental positions (Fig. 8) by iteratively modifying the calculated temperature distribution using  $k$  as adjusting parameter (see Fig. 7).